International Journal of Heat and Mass Transfer 156 (2020) 119860

Contents lists available at ScienceDirect

International Journal of Heat and Mass Transfer

journal homepage: www.elsevier.com/locate/hmt

Calibration of conductance channels and heat flux sharing in scanning thermal microscopy combining resistive thermal probes and pyroelectric sensors

M. Chirtoc[a,*], J. Bodzenta[b,*], A. Kaźmierczak-Bałata[b]

[a] Thermophysics Lab., ITheMM, Université de Reims Champagne Ardenne URCA, Moulin de la Housse, BP 1039, 51687 Reims, France
[b] Institute of Physics, Center for Science and Education, Silesian University of Technology, Konarskiego 22B, 44-100 Gliwice, Poland

ARTICLE INFO

Article history:
Received 14 October 2019
Revised 23 April 2020
Accepted 23 April 2020
Available online 19 May 2020

Keywords:
Nanoscale heat transfer
Scanning thermal microscopy
Thermal probe
Pyroelectric sensor
Thermal conductivity
3-omega method

ABSTRACT

The goal of this work is to establish the heat flux sharing among different heat exchange channels in scanning thermal microscopy (SThM), basing on experimental data. To this end, dc or modulated excitation with 3-omega detection at the third harmonic is applied to two types of resistive (Wollaston-, WThP and nanofabricated-, NThP) thermal probes. The main difference between the WThP and the NThP is the absence of a thermal coupling zone between the active zone and the heat sink in the WThP. Probe responsivities in dc or ac regime are defined, which depend only on total thermal conductance of probe-sample system. It is shown that in SThM it is not possible to discriminate between heat fluxes leaking across the air to the ambient and to the sample. Because of their interdependence, only their sum can be determined with the ThP alone. Replacing the sample by a pyroelectric heat flux sensor (PES), its 2-omega signal yields the ratio of the flux received through the contact to that received through the air. Eventually, the complete heat flux sharing among different channels is determined, for the studied high conductivity sample. For both probes, about 60 % of the dissipated power leaks through the cantilever to the probe holder. The heat flux through the contact represents 19.5 % for the WThP and 11.4 % for the NThP. The remaining heat flux is lost to the ambient or to the sample via the air. The corresponding thermal conductance values are determined in successive steps in vacuum (V), in air (A), out of contact (N) and in contact (C) using thermal quadrupole representations. The procedure requires only the calibration of the ThP and not that of the PES. For thermal conductivity measurements, the reference configuration (N) offers superior dynamic range to (A) one.

1. Introduction

Among many measuring techniques for thermal characterization on the nanoscale the scanning thermal microscopy (SThM) has become a mature investigation method [1,2]. Various applications relying on temperature-dependent phenomena benefit from a spatial resolution that is determined by the probe size and is not restricted by optical diffraction [3]. It reaches sub-100 nm in vacuum, while the temperature resolution is sub-0.1 K. Techniques combining SThM with micro-thermography, IR radiometry, scanning near field optical microscopy (SNOM) and thermoelastic detection have been reported in the past [4]. Early variants of SThM were based on a variety of thermal sensing effects [5]. The most often used thermal probes (ThPs) are the Wollaston wire probes (WThP) [6] having μm spatial resolution, batch fabricated nanolithographic thin film probes (NThP) using thermocouple [7,8] or resistive [9,10] elements that have ≈100 nm spatial resolution, and doped silicon V-shape resistive probes offering 10 nm spatial resolution [11,12].

The first calibration procedures were based on differential signal measurements with the tip in air (far from the sample) and in contact with the sample [6,13]. It was assumed that the temperature distribution in and around the ThP remains unchanged, and that the heat flux to the sample is proportional to its thermal conductivity *k*. Subsequent studies demonstrated that these assumptions are not valid and proposed as reference for static measurements the position of the tip just before contact [1]. Later this procedure called the double scan technique [14] was applied to the correction of SThM thermal maps. It was improved as the null-point technique [15] that cancels the heat flux across the contact

---

[*] Corresponding authors.
E-mail addresses: mihai.chirtoc@univ-reims.fr (M. Chirtoc), jbodzenta@polsl.pl (J. Bodzenta).

https://doi.org/10.1016/j.ijheatmasstransfer.2020.119860

Nomenclature

a	thermal diffusivity, m^2 s^{-1}
Bi	Biot number
C	electrical capacitance, F
d	width, m
F	form factor of temperature distribution
f	temperature oscillation frequency, Hz
g	reduced thermal conductance
G	thermal conductance, μW K^{-1}
h	heat exchange coefficient, W m^{-2} K^{-1}
I	excitation current, A
k	thermal conductivity, W m^{-1} K^{-1}
l	length, m
m	fin parameter, m^{-1}
P	electrical power or heat flux, W
Q	heat quantity, J
R	electrical resistance, Ω
R_1... R_5	thermal resistance, K μW^{-1}
r	radius, m
r_{el}	temperature coefficient of R, K^{-1}
S_n	normalized responsivity of thermal probe, W^{-1}
S_{PE}	responsivity of pyroelectric sensor, V W^{-1}
s	wire cross section, m^2
t	thickness, m
V	voltage signal, V
x	spatial coordinate, m

Greek symbols

θ	temperature increase, K
ω, 2ω, 3ω	angular frequency harmonics, s^{-1}
τ	time constant, s

Subscripts

0	reference quantity
a	air
h	probe holder
p	probe body
PE	pyroelectric sensor
sa	probe - sample interaction through air
sc	tip - sample contact
w	wire

Superscripts

V	in vacuum
A	in air, far from sample
N	just before contact, in air
C	in contact, in air

Abbreviations

NThP	nanofabricated thin film thermal probe
PES	pyroelectric sensor
SThM	scanning thermal microscopy
ThP	thermal probe
WThP	Wollaston thermal probe

and thus removes the uncertainty related to the interfacial thermal resistance. Recently, more elaborate calibration strategies have emerged [16].

In view of quantitative active SThM equipped with resistive ThPs, we approached the transfer functions of the instrument at three levels, corresponding respectively to the nano-scale, microscale and mesoscale:

(i) Thermophysical modeling of the relation between sample conductivity and total contact conductance, within the contact zone of the ThP [18,19].

(ii) Average transducer temperature as function of heat flux sharing among different conductance channels, in the active zone and coupling zone of the ThP [4,20,21]. The link with level (i) is through the contact conductance.

(iii) Relation between the electrical resistance of the active element and the (dc, ac, 2ω, 3ω, transient) signal processed by the SThM instrument [4,22–24]. The resistance-temperature calibration of the ThP allows the link with level (ii). The overall calibration curve is the product of the three transfer functions.

To address the level (ii) above, the heat flux distribution in the probe-sample system must be correctly known. While the conductance of the probe body can be easily determined in vacuum, other conductances of similar heat exchange channels are hard to separate [1]. In particular, we show that it is not possible to discriminate between the heat flux leaking across the air from the ThP to the ambient and the one transferred across the tens of μm thick air gap between ThP and sample. The latter is different from the ballistic conductance in air at the contact zone and is neglected in most cases [1,2]. However, the share of this channel to the global ThP-sample heat exchange can be significant [25,26]. This contributes among other geometrical factors to large deviations between the experimental heat exchange coefficient h and the much lower theoretical values that are based on macroscopic correlations [1]. In order to complete such missing information for a realistic heat flux balance in different ThPs, this work proposes a combined calibration methodology using a pyroelectric heat flux sensor (PES) instead of the sample. The comparative study focuses on the same commercially available resistive WThP and NThP as in Ref. [27]. First, current-voltage characteristics with dc excitation were performed with the ThPs in vacuum, in argon and in air, for calibration purposes. Second, classical 3ω experiments were performed with the ThPs in air, far from the sample, close to contact and in contact. The results of the two types of experiments were combined using the known fact that the dc and ac regimes are equivalent below a specified cut-off modulation frequency. Section 2 presents the principle of the association of a ThP with a PES. Section 3 contains the procedure for the deconvolution of conductances corresponding to various heat exchange channels. The experimental setup and the dc calibration of ThPs are described in Section 4. The conductance results, the heat flux sharing and a comparative discussion of WThP and NThP are presented in Section 5.

2. Principle of thermal probe - pyroelectric sensor association

In a typical calibration experiment of passive SThM the heat flux flows from the heated nanofabricated calibration device into the ThP [25]. In active SThM the ThP is the excitation source and the sensor in the same time. Due to small sample volume seen by the ThP, the relevant thermophysical property that is being measured is the thermal conductivity k [27]. In dc regime, the electrical power P dissipated by the heating element is converted into a heat flux that increases the ThP temperature by an amount θ and leaves the ThP through its total thermal conductance G given by:

$$\theta = P/G \tag{1}$$

This relation still holds for amplitude values of quantities in ac regime below a cut-off frequency. In this case, the temperature follows the power variation and heat transfer phenomena can be treated as quasi-static processes. Above the cut-off frequency the temperature amplitude decreases as $1/f$ and has a $\pi/2$ phase lag [21,24]. The 3ω method is a powerful electro-thermal method that uses the same (wire or metallic strip) transducer for simultaneous thermal excitation and temperature detection [29] and it has been extended to SThM operation [22,28]. Keeping only the periodic terms, the excitation current $I\sin(\omega t)$ generates a periodic power $-P\cos(2\omega t)$ which causes a temperature oscillation $-\theta\cos(2\omega t)$. Thus the temperature-dependent electrical resistance $R(\theta)=R_0[1-r_{el}\theta\cos(2\omega t)]$ will be also modulated at 2ω. In the end, the voltage across the heater contains a term $V_{3\omega}\sin(3\omega t)$ proportional to the temperature of the resistive element averaged over its length [29,30]:

$$V_{3\omega}=-\frac{r_{el}IR_0\theta}{2}=-\frac{r_{el}IR_0P}{2G}=-\frac{r_{el}I^3R_0^2}{4G} \tag{2}$$

since $P=I^2R_0/2$. Here r_{el} is the temperature coefficient of electrical resistivity of the heating element material. Eq. (2) shows that the 3ω signal measures the total ThP thermal conductance if the heat flux source is constant. It has opposite phase relative to the excitation current.

A pyroelectric sensor (PES) generates a current that is proportional to the rate of temperature change $d\theta_{\mathrm{PE}}/dt$ integrated over its volume [31]. The temperature increment $\theta_{PE}(t)$ is generated by a time-varying heat quantity $Q(t)$ that reaches the sensor. Its rate represents a heat flux P_{PE}. With the 3ω method, $Q(t)$ oscillates at 2ω, and so does the PE current. The input resistance R of the lock-in amplifier in parallel with the capacitance C of the PES forms a low-pass filter with a time constant $\tau=RC$. Depending on frequency, the PES works in current mode ($2\omega<1/\tau$), or in voltage mode ($2\omega>1/\tau$), having different frequency dependences [32]. In both cases, the PE voltage $V_{2\omega}$ measured by the lock-in is proportional to the PE current at a given frequency, and then:

$$V_{2\omega}\propto\frac{d\theta_{PE}}{dt}\propto\frac{dQ}{dt}=P_{PE} \tag{3}$$

Due to the volume integration of θ_{PE}, the response of the PES sensor is fast and depends only on the thermal transfer time across the top Au electrode. Eq. (3) proves that the PES can be used as a sensitive heat flux sensor in modulated active SThM. In a first experiment associating a WThP with a PES, the sample was a polymer layer deposited on sensor's electrode. The PES measured the attenuation and the phase lag of the thermal wave in a transmission configuration. Thus the cross-plane thermal diffusivity has been mapped [33].

The Fig. 1 illustrates the principle of combined SThM-PES setup used in this work. The goal is to determine all conductance channels using $V_{3\omega}$ and $V_{2\omega}$ signals and eventually to establish the complete heat flux balance of the ThP. In Fig. 1, a flux P_{PE} flows from the ThP to the PES not only through the contact thermal conductance G_{sc}, but also through air conductance G_{sa}. Several authors have observed that the ThP signal changes in the presence of the sample long before the contact is reached [2,17]. This suggests that a fraction of the flux is transferred across the ThP-sample air gap over a longer distance range than the size of the contact [1,25,26].

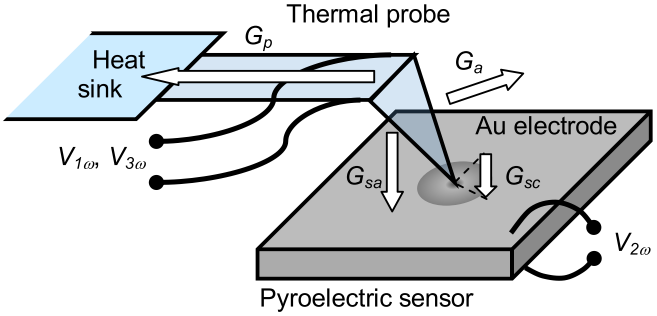

Fig. 1. Association of a SThM thermal probe (WThP or NThP) with a pyroelectric heat flux sensor (PES) used as a sample. Arrows indicate heat loss channels from the heated zone through the cantilever to the probe base - G_p, to the ambient air - G_a, through the air to the PES - G_{sa}, and across the contact zone to the PES - G_{sc}.

The corresponding conductance G_{sa} cannot be distinguished from the conductance G_a to the ambient by using the information from the ThP. Only their sum is experimentally accessible, while G_a is not constant in different configurations. It is one of the goals of this work to measure G_{sa}, which is comparable with or even larger than G_{sc}, as will be shown further below. The analysis of the structure of G_{sc} pertains to level (i) mentioned in Section 1. It contains possible contributions from solid contact, water meniscus, radiative transfer and short-range ballistic conductance through air [1].

Crucial for the calibration of resistive ThPs with distributed sensor is the fact that the signal is proportional to the average temperature of the heating element, while the sample is excited by the apex temperature. Depending on ThP architecture, the temperature field in the active zone can be approached analytically by the fin theory [28], by finite element numerical computation [13,21], or by a simplifying isothermal assumption.

3. Stepwise procedure for the determination of thermal conductances

The total thermal conductances in different configurations (in vacuum, in air, no contact and in contact) are determined experimentally from ThPs dc signals according to Eq. (33) of Section 4, as:

$$G^{V,A,N,C}=r_{el}P/(\Delta R/R_0) \tag{4}$$

Similarly, the conductances can be determined from $V_{3\omega}$ signals with Eq. (2). The deconvolution of different conductances of heat exchanges in the two probe-sample systems is detailed in the next sections.

3.1. Wollaston probe - pyroelectric sensor (WThP/PES) system

3.1.1. Temperature profile of the heating element

Resistive ThPs have mirror symmetry in the longitudinal direction. For the WThP, the half-length $l/2$ of the heating element is equivalent to a cylindrical fin attached to a wall [29,30] (Fig. 2). The temperature profile $\theta(x,f)$ along the suspended wire excited by ac current is described by a form factor $F(x,f)=\theta(x,f)/\theta_0$ where $\theta_0=(P/2)/G_{p0}$. The normalizing quantity $G_{p0}=k_w s/(l/2)$ is the dc thermal conductance in the axial direction of one arm of the ThP, with k_w the thermal conductivity and $s=\pi r_w^2$ the cross section of the wire. With the following parameters of the $\mathrm{Pt_{90}Rh_{10}}$ wire: $l/2=100$ μm, $2r_w=5$ μm, $k_w=38$ $\mathrm{Wm^{-1}K^{-1}}$, one obtains $G_{p0}=7.46$ μW/K ±20 %. G_{p0} would be the internal conductance if the power source $P/2$ was concentrated at the apex of the ThP (at $x=0$) (Fig. 2). It is reasonably assumed that the holders of the wire (at $x=l/2$) are nearly-ideal heat sinks with $G_h\rightarrow\infty$, since $\theta(x=l/2)/\theta(x=0)\approx0.005$ [34]. With this simplifying assumption, the form factor has the expression [4]:

$$F(x,f)=\frac{1}{(ml/2)^2}\left\{1-\frac{\left[(ml/2)+g_{sc}\left(1-e^{-ml/2}\right)\right]e^{mx}+\left[(ml/2)-g_{sc}\left(1-e^{ml/2}\right)\right]e^{-mx}}{ml\cosh(ml/2)+2g_{sc}\sinh(ml/2)}\right\} \tag{5}$$

with $m^2=g_a/(l/2)^2+j2\pi f/a_w$ the fin parameter and a_w the wire thermal diffusivity. The parameter $g_a=(G_a/2)/G_{p0}$ is the reduced lateral thermal conductance through the air, distributed along the wire length and $g_{sc}=(G_{sc}/2)/G_{p0}$ is the reduced contact thermal conductance between the ThP and the sample, localized at the apex. For WThP, Eq. (5) predicts a parabolic temperature profile $\theta(x,f)$, which has been experimentally validated by IR thermography and micro-thermocouple profiling [13,22,35]. In the radial di-

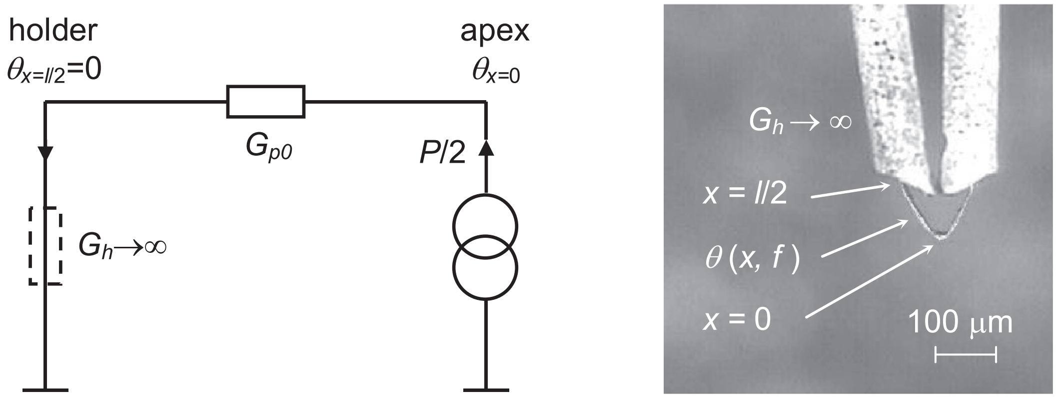

Fig. 2. (left) Thermal quadrupole representation of the normalizing conductance G_{p0} for the half-length ($l/2$) Wollaston probe. The virtual power source is localized at the apex at $x = 0$. The real distribution of the power source is depicted in Fig. 3. (right) micrograph of the heating element supported by silver prongs (see also [36]).

rection, the wire is thermally thin ($Bi \approx 3 \cdot 10^{-4}$), implying a uniform temperature profile.

The thermal frequency f corresponds to 2ω, with ω the electrical angular frequency of the excitation current. The frequency dependence of $F(x,f)$ has been studied before [22,23,28]. The resistive thermal probes (ThPs) for SThM are sensitive to sample thermal conductivity k only in the quasi-static regime below a cut-off frequency f_0, with $f<f_0$, (about 100 Hz for WThP and 1 kHz for NThP). In this case and for low excitation level, $m = (g_a)^{1/2}/(l/2)$ and is independent of frequency and of thermal diffusivity of the wire. From Eq. (5), the form factor averaged over length $l/2$ is obtained as [20]:

$$\langle F(g_a, g_{sc})\rangle = \frac{1}{g_a}\left(1 - M\frac{1+g_{sc}M_{1/2}}{1+g_{sc}M}\right) \tag{6}$$

In particular, at the two ends $F_{x=l/2} = 0$, while at the apex:

$$F_{x=0}(g_a, g_{sc}) = \frac{MM_{1/2}}{2(1+g_{sc}M)} \tag{7}$$

In Eqn 7, $M = [\tanh(g_a{}^{1/2})]/(g_a{}^{1/2})$ and $M_{1/2} = [\tanh(g_a{}^{1/2}/2)]/(g_a{}^{1/2}/2)$. In the presence of the sample, the lateral heat flux is split in two parts corresponding to a smaller conductance $G_a/2$ to the ambient air and a conductance $G_{sa}/2$ to the sample through the air gap (see also Section 2). Their relative weight depends on measurement configuration. In vacuum, $g_a = 0$ and from Eq. (6), $<F>$ varies between 1/3 (no contact) and 1/12 (perfect contact). It results that the maximum dynamic range of resistive wire ThP is $DR = <F_{max}> / <F_{min}> = 4$ [4,20].

3.1.2. Thermal quadrupole model

The $V_{3\omega}$ signal from the ThP is proportional to the average temperature profile θ and hence to $<F(g_a, g_{sc})>$. In the present work the ThP was driven by low level ac current with constant amplitude, such that the variation of heater resistance due to dc temperature increase can be neglected. Therefore, the heat flux source is considered as a constant power source P. Then from Eq. (2), the lumped thermal conductance G of the ThP (for full length l) is related to its signal or to its temperature as:

$$G = \frac{2G_{p0}}{<F>} \propto \frac{1}{V_{3\omega}} \propto \frac{1}{\theta} \tag{8}$$

The total conductance G incorporates all heat exchange channels between the ThP and its surroundings, but it is not a simple sum of different conductances. These are intricately combined in the average form factor $<F>$ according to Eq. (6). One cannot define a true, intrinsic conductance of the ThP because the power sources and heat flow channels are distributed according to the ThP design. Nevertheless, in all experimental configurations one may determine an effective conductance G_p of the ThP body by subtracting all other conductances from G:

$$G_p = G - \sum G_i \tag{9}$$

The resulting G_p of Eqn 9 satisfies the heat flux conservation law. The thermal quadrupole model of the WThP is shown in Fig. 3.

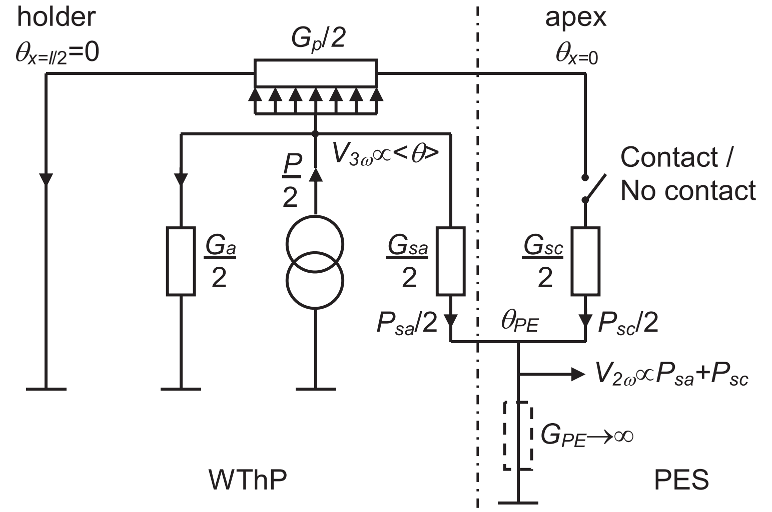

Fig. 3. Thermal quadrupole model of half-length Wollaston ThP. The sample is a pyroelectric sensor (PES). The power source is uniformly distributed along the heating element between the apex at $x = 0$ and the wire prongs at $x = l/2$.

3.1.3. Wollaston probe (WThP) heat flux balance

Total conductances $G^{V,A,N,C}$ are determined with Eq. (4). Three experimental steps are necessary to establish the sharing of heat fluxes through G_p, G_a+G_{sa}, and G_{sc} conductances: in vacuum (V), no contact (N) and in contact (C). An optional step (A) with the ThP in air or in another gas, far from the sample, can be performed in order to study the variations of G_p and G_a with the experimental conditions. The following discussion pertains to the full length l of the heating element and is based on the theoretical value of G_{p0}. The $<F>$ factor in each step is proportional to respective dc or ac signals (Eq. 8). It is determined relative to the value $<F^V>=1/3$ in vacuum, which results from Eq. (6) for $g_a\to 0$ and $g_{sc}=0$.

Step (V). The ThP is suspended in vacuum. In Fig. 3 only conductance G_p is present which represents the total conductance G^V of heat diffusion from the ThP. Then with Eq. (8) one obtains:

$$G^V = G_p^V = 2G_{p0}/<F^V>=6G_{p0} \tag{10}$$

Step (A). The ThP is suspended in air. In Fig. 3 only conductances G_p and G_a are present which form the total conductance G^A of heat diffusion from the ThP. Then with Eq. (8) one obtains:

$$G^A = G_p^A + G_a^A = 2G_{p0}/<F^A> \tag{11}$$

and:

$$G_a^A = 2G_{p0}g_a^A, \quad G_p^A = G^A - G_a^A \tag{12}$$

The g_a^A parameter is determined by numerical inversion of Eq. (6) where $g_{sc}=0$.

Step (N). The ThP is brought closely to the sample surface, just before contact. The configuration is analogous to that in step (A), the only change being an additional conductance G_{sa} through the air gap between the ThP and the sample surface (see Fig. 3). Eqs. (11) and (12) become Eqn 13 and Eqn 14:

$$G^N = G_p^N + G_a^{N,C} + G_{sa}^{N,C} = 2G_{p0}/<F^N> \tag{13}$$

and:

$$G_a^{N,C} + G_{sa}^{N,C} = 2G_{p0}g_a^{N,C}; \quad G_p^N = G^N - \left(G_a^{N,C} + G_{sa}^{N,C}\right) \tag{14}$$

As in step (A), the $g_a^{N,C}$ parameter is determined by numerical inversion of Eq. (6) where $g_{sc}=0$. The total conductance through the air $G_a^{N,C}+G_{sa}^{N,C}$ is larger than G_a^A. Also, $G_a^{N,C}\neq G_a^A$ because now part of the free space around the ThP is occupied by the sample. The superscripts $^{N,\,C}$ indicate that the respective quantities remain unchanged in the next step (C) below because the tip-sample relative distance is almost the same.

Step (C). The ThP is put in contact with the sample. In Fig. 3 all conductances are present. Since G_{sc} is not connected to the same temperature as the other conductances, the following expression includes a correction by the ratio of apex temperature to average temperature:

$$G^C = G_p^C + G_a^{N,C} + G_{sa}^{N,C} + \left(\theta_{x=0}^C/\theta^C\right)G_{sc} = 2G_{p0}/<F^C> \tag{15}$$

where:

$$G_{sc} = 2G_{p0}g_{sc} \tag{16}$$

Using the $g_a^{N,C}$ value from step (N), the parameter g_{sc} is found by numerical inversion of Eq. (6). The sum $G_a^{N,C}+G_{sa}^{N,C}$ being the same as in step (N), it follows that:

$$G_p^C = G^C - \left(G_a^{N,C} + G_{sa}^{N,C}\right) - \left(\theta_{x=0}^C/\theta^C\right)G_{sc} \tag{17}$$

In this step, G_{sc} is determined basing on quantities found in the previous steps. Note that only the total heat flux through the air via $G_a^{N,C}+G_{sa}^{N,C}$ can be determined using the signal from the ThP. This indetermination will be raised in the next Section using additional information from the PES.

3.1.4. Pyroelectric sensor (PES) heat flux balance

Two experimental steps are necessary to establish the sharing of heat fluxes to the sample through G_{sa} and G_{sc} conductances.

Step (N). The ThP is just before contact. In Fig. 3 only conductances G_p, G_a and G_{sa} are present. The PES signal $V_{2\omega}^N$ is proportional to the heat flux P_{sa}^N flowing through conductance G_{sa}:

$$V_{2\omega}^N \propto P_{sa}^N = \theta^N G_{sa}^{N,C} = \frac{PG_{sa}^{N,C}}{G^N} \tag{18}$$

Step (C). The ThP is in contact with the sample, i.e., with the PE sensor surface. In Fig. 3 all conductances are present. Note that G_{sc} is connected to a higher temperature than G_{sa}, that is to the apex temperature $\theta_{x=0}^C$. The PE signal $V_{2\omega}^C$ is proportional to the heat flux $P_{sa}^C+P_{sc}^C$ flowing through conductances G_{sa} and G_{sc}:

$$V_{2\omega}^C \propto P_{sa}^C + P_{sc}^C = \theta^C G_{sa}^{N,C} + \theta_{x=0}^C G_{sc} = \frac{PG_{sa}^{N,C}}{G^C}\left(1 + \frac{\theta_{x=0}^C}{\theta^C}\,\frac{G_{sc}}{G_{sa}^{N,C}}\right) \tag{19}$$

Writing the ratio of Eqs. (19) and (18), one obtains:

$$\frac{V_{2\omega}^C}{V_{2\omega}^N} = \frac{P_{sa}^C + P_{sc}^C}{P_{sa}^N} = \frac{G^N}{G^C}\left(1 + \frac{\theta_{x=0}^C}{\theta^C}\,\frac{G_{sc}}{G_{sa}^{N,C}}\right) \tag{20}$$

From Eq. (20), the ratio of conductances through the contact and through the air, which link the ThP to the PES, is given by:

$$\frac{G_{sc}}{G_{sa}^{N,C}} = \frac{\theta^C}{\theta_{x=0}^C}\left(\frac{V_{2\omega}^C}{V_{2\omega}^N}\,\frac{G^C}{G^N} - 1\right) = \frac{<F^C>}{F_{x=0}^C}\left(\frac{V_{2\omega}^C}{V_{2\omega}^N}\,\frac{V_{3\omega}^N}{V_{3\omega}^C} - 1\right) \tag{21}$$

In the last part of Eq. (21) use was made of Eq. (8). It clearly shows that the sharing of heat fluxes to the sample can be obtained by combining the signals $V_{3\omega}$ from the ThP with the ones from the PE sensor, $V_{2\omega}$. The result is independent of the measurement in air far from the sample (step A). The conductance $G_{sa}^{N,C}$ is determined basing on Eqs. (16) and (21). Finally, $G_a^{N,C}$ is derived by subtraction of $G_{sa}^{N,C}$ from their sum determined in Eq. (14). Thus the PES allows differentiating the heat flux lost from the ThP to the ambient through $G_a^{N,C}$, from the one transferred to the sample through the air gap via $G_{sa}^{N,C}$.

3.2. Nanofabricated probe - pyroelectric sensor (NThP/PES) system

3.2.1. Thermal quadrupole model

The NThP has a more intricate architecture than the WThP. Starting from the apex to the holder, the heat transfer to air changes from ballistic to slip and diffusive regime [25], and the exchange coefficient h varies continuously by orders of magnitude (see estimations in Section 5.2). Therefore, a form factor analogue to Eq. (5) is difficult to establish. The model proposed in Ref. [37] assumes an unrealistic heat sink condition at the ends of the heating element. Contrary to the WThP, in the NThP the active zone is separated from the coupling zone, and one can reasonably assume that the conductance G_p of the latter is less affected by the redistribution of the temperature field in the heater under different operating conditions. In a first approximation it will be assumed that the active zone is isothermal, in particular that $\theta_{x=0}=<\theta>$. A correction will be applied in Section 5.2 to the obtained G_{sc} value.

The quadrupole model of the NThP consisting of several thermal RC cells was developed in Ref. [21]. The analytical transfer function formulated in terms of time constants and dimensionless thermal resistance ratios describes its frequency characteristics. At low frequency (quasi-static regime), capacitive thermal impedances can be neglected. This allows grouping several conductances to the ambient air from different zones of the ThP into a single one, G_a. The resulting model of the NThP reduces to that of Fig. 4a containing discrete circuit elements. Here G_p is the conductance of the cantilever (characteristic length ≈100 μm) and is constant. It acts as a coupling zone between the active zone (characteristic length

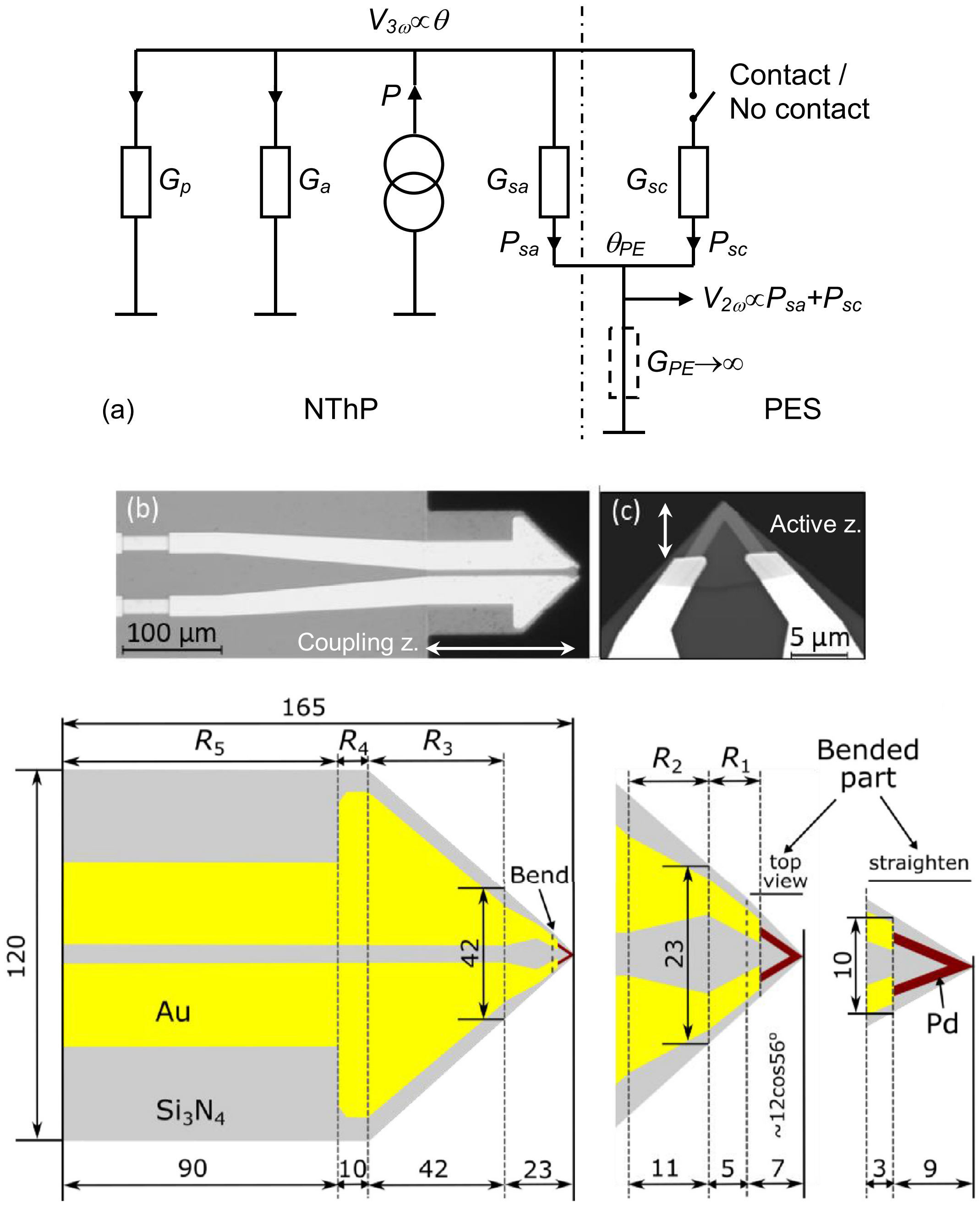

Fig. 4. (a) Thermal quadrupole model of full-size nanofabricated probe (NThP). The sample is a pyroelectric sensor (PES). (b) Micrograph of KNT-SThM-1an NThP [38]. The two strips on the probe base are balance resistors. (c) SEM image of probe apex. (d) Geometry of regions (in μm) having thermal resistances R_1...R_5. Yellow strips are gold pads (color on-line). The power source P is localized in the V-shaped Pd strips of the active zone. (For interpretation of the references to color in this figure legend, the reader is referred to the web version of this article.)

$\approx$10 μm) containing the Pd heating element and the probe holder equivalent to a heat sink (Fig. 4b-d).

The ThP consists of a $t = 400$ nm thick Si_3N_4 substrate slab having $l_p = 165$ μm in length and $d = 120$ μm width. The light strips (Fig. 4b) are $t = 140$ nm thick gold connection pads to the 40 nm thick V-shaped Pd strip (Fig. 4c) that is the heating element. Conductance G_p can be calculated basing on the full-size geometry of Fig. 4d in a similar way as in Ref [21] and by considering the conduction through the gold pads as well. The thermal resistances of trapezoidal and rectangular substrate regions in the direction of the heat flow are respectively $R_{1...3} = [l/(kt)]\ln(d_2/d_1)/(d_2\text{-}d_1)$ and $R_{4,5} = l/(ktd)$ with l, d_1, d_2, and d the length and widths of each region. The resistances of gold layers were evaluated by multiplying these expressions by a coverage factor. For each region, the resistance of substrate and gold layer in parallel was calculated, and finally these resistances were summed up yielding 0.090 K/μW for the trapezoidal region and 0.045 K/μW for the rectangular one. To that, the average resistance of the active region (=0.125 K/μW according to a model mentioned in Section 5.2) was added. The resulting conductance of the whole ThP is $G_p = 3.85$ μW/K ±20 %, with $k = 10$ $Wm^{-1}K^{-1}$ for Si_3N_4 and 200 $Wm^{-1}K^{-1}$ for Au. The latter value is 30 % less than 315 $Wm^{-1}K^{-1}$ for bulk Au, due to phonon confinement effect in the thin gold layer and was calculated according to the model in Ref. [18]. The substrate conductivity can be off by several $Wm^{-1}K^{-1}$ but as we shall see, it does not impact strongly the results because most of the flux flows in the metal. The obtained ThP conductance is consistent with the theoretical estimation $G_p = 4.42\ \mu$W/K [25] and it is of the same order as the experimental value of 1.92 μW/K [27]. Due to high conductivity of gold, the contact pads channel three times more heat flux than the substrate. Therefore, the effect of the uncertainty in the conductivity of the substrate is reduced in the same proportion. The heat flux through the pads is controlled by Au resistance R_1 which represents 40 % of total resistance of the Au thermal path. The heat management in this NThP might be optimized by decreasing the resistance of the active zone and increasing resistances R_1... R_5 of the coupling zone.

3.2.2. Nanofabricated probe (NThP) heat flux balance

The procedure is analogous to the one for WThP and contains the (V), (A), (N) and (C) steps, with the difference that G_p is unchanged in different ambient or sample contact conditions.

Step (V). The ThP is suspended in vacuum. In Fig. 4a only conductance G_p is present. Then the total thermal conductance G^V of the ThP is simply:

$$G^V = G_p \tag{22}$$

Step (A). The ThP is suspended in air. In Fig. 4a only conductances G_p and G_a are present which form the total thermal conductance G^A:

$$G^A = G_p + G^A_a \tag{23}$$

whence:

$$G^A_a = G^A - G_p \tag{24}$$

Step (N). The ThP is brought closely to the sample surface, just before contact. The configuration is analogous to that in step (A), with an additional conductance G_{sa} through the air gap between the ThP and the sample surface (see Fig. 4a). Eqs. (23) and (24) become Eqn 25 and Eqn 26:

$$G^N = G_p + G^{N,C}_a + G^{N,C}_{sa} \tag{25}$$

and the total conductance through air is obtained as:

$$G^{N,C}_a + G^{N,C}_{sa} = G^N - G_p, \tag{26}$$

which is larger than G^A_a.

Step (C). The ThP is put in contact with the sample. In Fig. 4a all conductances are present:

$$G^C = G_p + G^{N,C}_a + G^{N,C}_{sa} + G_{sc} \tag{27}$$

The sum $G^{N,C}_a + G^{N,C}_{sa}$ of Eqn 27 being the same as in step (N), it follows that:

$$G_{sc} = G^C - G^N \tag{28}$$

As in the case of the WThP, the discrimination between $G^{N,C}_a$ and $G^{N,C}_{sa}$ requires additional information available from the PE sensor.

3.2.3. Pyroelectric sensor (PES) heat flux balance

As in Section 3.1.4., two experimental steps are necessary to establish the sharing of heat fluxes to the sample through G_{sa} and G_{sc} conductances.

Step (N) is identical to step (N) of Section 3.1.4. but Eq. (18) now refers to Fig. 4a.

Step (C) is more straightforward than step (C) of Section 3.1.4 because in Fig. 4a all conductances are connected to the same temperature. Then Eqs. (19-21) reduce to following Eqs. (29), Eqn 30 and (31):

$$V^C_{2\omega} \propto P^C_{sa} + P^C_{sc} = \theta^C\left(G^{N,C}_{sa} + G_{sc}\right) = \frac{PG^{N,C}_{sa}}{G^C}\left(1 + \frac{G_{sc}}{G^{N,C}_{sa}}\right) \tag{29}$$

$$\frac{V^C_{2\omega}}{V^N_{2\omega}} = \frac{P^C_{sa} + P^C_{sc}}{P^N_{sa}} = \frac{G^N}{G^C}\left(1 + \frac{G_{sc}}{G^{N,C}_{sa}}\right) \tag{30}$$

$$\frac{G_{sc}}{G^{N,C}_{sa}} = \frac{V^C_{2\omega}}{V^N_{2\omega}}\frac{G^C}{G^N} - 1 = \frac{V^C_{2\omega}}{V^N_{2\omega}}\frac{V^N_{3\omega}}{V^C_{3\omega}} - 1 \tag{31}$$

The conductance $G^{N,C}_{sa}$ is determined basing on Eqs. (28) and (31). Finally, $G^{N,C}_a$ is derived as in Section 3.1.4.

In conclusion, the outlined stepwise procedure allows determining G_p, G_a+G_{sa} and G_{sc} from ThP signals, and the ratio G_{sc}/G_{sa} from PES signals. Eventually, all individual conductances can be derived by combining the two sets of results.

4. Experimental setup and thermal probe calibration

The ThP can be excited by dc or ac current, or by a combination of the two [24]. In this study dc and ac measurements are equivalent because the thermal diffusion length is larger than $l/2$ (low frequency, quasi-static regime). With dc excitation, the resistance is expressed as:

$$R(\theta) = R_0(1 + r_{el}\theta) \tag{32}$$

and with Eq. (1), the relative resistance change is:

$$\frac{\Delta R}{R_0} = \frac{r_{el}P}{G} \tag{33}$$

From Eq. (33), the plot $\Delta R/R_0$ *vs.* P has a slope r_{el}/G which allows determining the absolute value of total thermal conductance G.

The dc measurements were carried out with Keithley 6221 current source and Agilent 34405A multimeter, with currents varied from 2 mA to 40 mA for WThP and from 0.1 mA to 2.0 mA for NThP. The measured resistance ($\geq$ 3.5 Ω) of the WThP includes the resistance of leads to ThP base and that of Ag prongs. Therefore, the nominal value $R_0 = 2.1$ Ω of the heating element was used for data processing. The measured resistance of the NThP extrapolated to zero current (424 Ω) includes two ballast resistors of 100 Ω each and thus $R_0 = 224$ Ω. For $Pt_{90}Rh_{10}$ alloy of the WThP wire, $r_{el} = 1.66 \bullet 10^{-3}$ K^{-1} is the nominal value [13] while for the Pd strip of the NThP, $r_{el} = 1.2 \bullet 10^{-3}$ K^{-1} was measured [37]. The probes were mounted in a small air-tight chamber allowing measurements in vacuum ($\approx 5 \bullet 10^{-2}$ Pa) and in controlled atmospheres (argon, air). Using Eq. (32), the maximum temperature increase in vacuum was $\theta = 112$ K for WThP and 225 K for NThP. Only the power P dissipated by the heating element is considered. The processed results are shown in Fig. 5. The respective slope values $(\Delta R/R_0)/P$ are gathered in Tables 2 and 3. The linear fits in Fig. 5a do not pass exactly through the origin because of errors in measuring small resistance variations ΔR (close to the origin) of a resistor R_0 having a few Ohms. Another cause might be the deviation from nominal value of R_0. If the intercepts of the linear fits for WThP are set to 0, their slopes increase by 7 %, which is within the specified uncertainty. The results in Fig. 5 are possibly subject to large variability from one ThP to another, which limits the modeling to the studied probes. Detailed description of the ThPs can be found elsewhere [25,34].

The ac measurements in air were carried out in two configurations. The WThP was placed in series with a 47 Ω resistor, in one leg of a Wheatstone bridge. Since R_0 has a much smaller value, constant current operation can be assumed ($I = 5.0$ mA effective). The ac excitation at 10 Hz was provided by the internal reference oscillator of a SR865 lock-in amplifier which was tuned to the 3rd harmonic and measured the $V_{3\omega}$ signal across the bridge. Prior to the measurements, the bridge was balanced at the fundamental frequency. The NThP was connected directly to the output of the

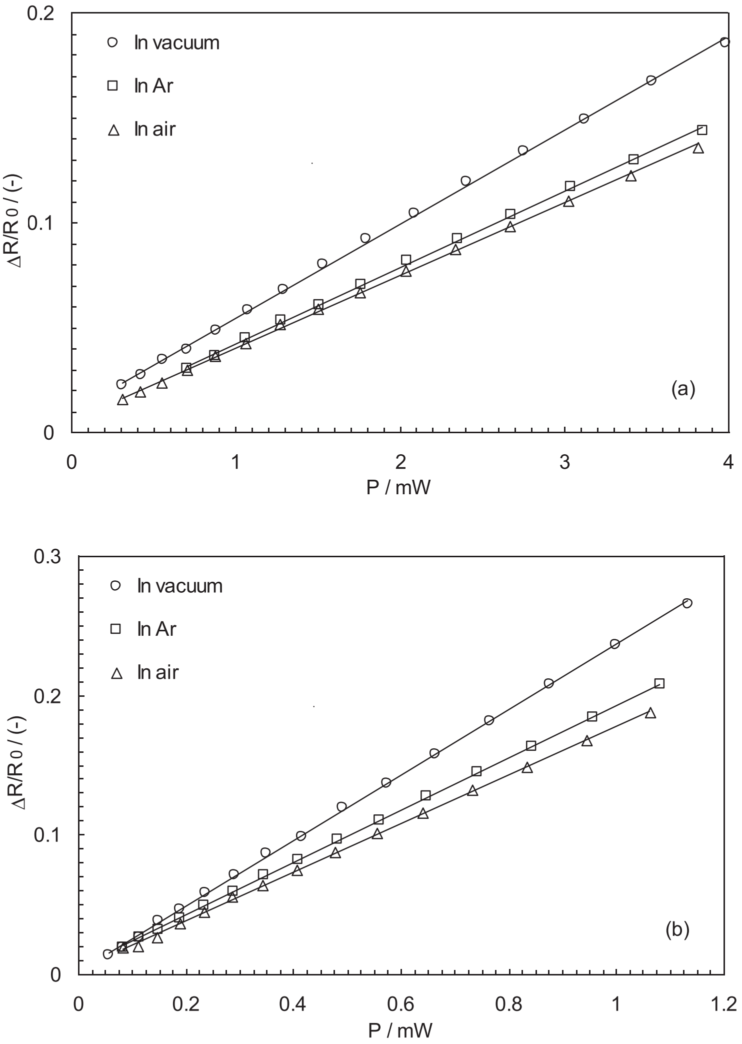

Fig. 5. Relative changes of ThP electrical resistance *vs* dissipated power measured for (a) WThP and (b) NThP in vacuum (V), in argon (Ar) and in air (A). Straight lines are fits having slope values $(\Delta R/R_0)/P = 44.7\ \text{W}^{-1}$, $36.2\ \text{W}^{-1}$, $34.4\ \text{W}^{-1}$ for WThP, and $234\ \text{W}^{-1}$, $188\ \text{W}^{-1}$, $174\ \text{W}^{-1}$ for NThP (±10 %).

Keithley 6221 current source ($I = 1.5$ mA effective) that was sinusoidally modulated at 80 Hz. The $V_{3\omega}$ probe voltage was measured by a SR830 lock-in amplifier synchronized with the current source, and tuned to the 3rd harmonic. In the quasi-static regime, the average temperature increase at the contact equals the amplitude of the temperature modulation. It can be calculated with Eq. (1), with the G_{sc} values of Tables 2 and 3, and with the heat flux sharing of Fig. 7. The result is 0.42 K ±20 % for WThP and 28.4 K ±20 % for NThP. The higher excitation level for the NThP was necessary due to very low $V_{2\omega}$ signal from the PES, which decreases with increasing frequency.

The ThPs were mounted into a XE-70 scanning microscope (Park Inc.). Its z-stage allows for precise control of the probe position relative to the sample. In both cases a 200 μm thick pyroelectric PZT ceramic slab ($k = 1.1\ \text{Wm}^{-1}\text{K}^{-1}$) coated with ≈1 μm thick gold electrodes ($k = 260\ \text{Wm}^{-1}\text{K}^{-1}$) was used as a high thermal conductivity sample (Fig. 1). The latter value is 18 % less than that for bulk gold due to phonon confinement effect and was calculated according to Ref. [18]. The effective conductivity of this multilayer sample measured by the WThP and NThP depends on the respective effective contact radius i.e., 1 μm and 100 nm. Using the approach of Ref. [18] for the calculation of the constriction thermal resistance of layered samples, one estimates the sample conductivities seen by the WThP and NThP as $k = 63\ \text{Wm}^{-1}\text{K}^{-1}$ ±10 % and $k = 195\ \text{Wm}^{-1}\text{K}^{-1}$ ±5 %, respectively. The $V_{2\omega}$ signal was fed to the 10 MΩ input impedance of the lock-in amplifier tuned to the 2nd harmonic. This resistance in parallel to the PES capacitance $C = 1$ nF yields an electrical time constant $\tau = 10$ ms. The PES does not need to be calibrated since only relative signal values are required.

The $V_{3\omega}$ and $V_{2\omega}$ signals in air (configuration A) were measured with the ThPs more than 3 mm apart from the sample. Upon approaching the sample, the signals in contact (C) correspond to values just after the snap to contact. The signals (N) correspond to a position just before contact and were obtained by extrapolation of the approach curve to position (C).

A normalized responsivity S_n [W^{-1}] which is independent of the excitation conditions can be determined from Eq. (2) for ac regime as:

$$S_n(ac) = \frac{2V_{3\omega}}{V_0}/P = \frac{4V_{3\omega}}{I^3R_0^2} = \frac{r_{el}}{G} \qquad (34)$$

and from Eq. (33) for the dc regime as:

$$S_n(dc) = \frac{\Delta(R)}{R_0}/P = \frac{r_{el}}{G} \qquad (35)$$

Table 1
Experimental responsivities $S_n(ac)$ and $S_n(dc)$ and theoretical one $S_n(th)$ of WThP and NThP in vacuum (V) (±20 %) calculated with parameters values specified in Sections 3.1.1, 3.2.1 and 4. Conductance G^V is obtained from Eqs. (10) and (22). $V_{3\omega}^V$ values were scaled following the $(\Delta R/R_0)/P$ levels in Tables 2 and 3.

ThP type	$S_n(ac)$ / W^{-1}	$S_n(dc)$ / W^{-1}	$S_n(th)$ / W^{-1}
WThP	32.2	44.7	37.1
NThP	156	234	264

Both experimental responsivities are equal to the theoretical responsivity $S_n(th)$ (last equalities), which is a direct measure of total thermal resistance ($1/G$) in a given tip-sample configuration. Therefore it can serve for intercomparison of quantitative SThM data obtained in different experimental conditions and for the link between levels (ii) and (iii) mentioned in Section 1.

For the same ThP type, the responsivities in Table 1 agree quite well, except $S_n(ac)$ of NThP. This might be due to the fact that the conductance G in ac and dc regimes is not really the same due to additional heating by the ballast resistors. Also, the temperature coefficient r_{el} of metals decreases with increasing temperature. In ac experiments, a high excitation current was necessary for the NThP because the PES signal was low, hence the average temperature of the NThP was high. In contrast, the slopes of Fig. 5b were determined at medium dc excitation current and the average temperature of the NThP was lower. As a result, the real r_{el} value in Eq. (34) is lower than that in Eq. (35), which may also explain why $S_n(ac) < S_n(dc)$.

The responsivity of the PES as a fluxmeter is a fixed parameter, $S_{PE} = V_{2\omega}/(P_{sa}+P_{sc})$ (amplitude values). With the P_s fraction of Fig. 7 and from total power amplitude $P = I^2R_0/2$, one obtains for WThP-PES in contact, S_{PE} = 1.73 V/W (in voltage mode on 10 MΩ load resistor, at $2f = 20$ Hz).

5. Results and discussion

5.1. Wollaston probe (WThP)

The calculation of quantities in Table 2 starts with the determination of $<F>$ values in configurations (A), (N) and (C) using its theoretical value of 1/3 in vacuum (V), scaled by the ratios of respective dc or ac signals measured from the WThP (Eq. 8). Total conductances G are obtained from Eq. (4). Other conductances are expressed as function of normalizing conductance G_{p0}. The experimental value $G_{p0} = 6.19$ μW/K ±10 % obtained with Eq. (10) compares well with the theoretical value mentioned in Section 3.1.1. The difference can be explained by the variability of wire length and radius, since the WThPs are manufactured manually. The conductances G_p are obtained with Eqs. (12), (14), (17) and G_{sc} with Eq. (16), using only the WThP data. G_{sa} is determined with Eq. (21) and G_a with Eqs. (12), (14), using also the PES data. As one can see, conductance G_p is not the same in different configurations because the temperature profile along the wire changes as well, according to $<F>$ factor (which is directly related to $V_{3\omega}$ signal, Eq. 8). For measurements in air, G_p varies between 39.0 and 46.5 μW/K (+22 %), depending on sample properties. Using a non-contact SThM mode [39], a similar variation between 47 and 62 μW/K (+32 %) could be derived for similar conditions. The fact that G_a and G_{sa} remain unchanged in (N) and (C) configurations is consistent with the principle of the double scan technique [14].

The value of G_a in air divided by the lateral area $2\pi r_w l$ of the wire yields the equivalent exchange coefficient $h = 2960$ Wm^{-2}K^{-1} ±30 %, in excellent agreement with $h = 3000$ [40]. These are consistent with a value of 2300 Wm^{-2}K^{-1} determined experimentally [34,41], which is still three times higher than that predicted by usual correlations for long (macroscopic) cylinders. In the presence of the sample, the increased G_a+G_{sa} yields even larger h values thus confirming the assumption of Section 4.4 in Ref. [1]. The total contact conductance $G_{sc} = 12.1$ μW/K is comparable with the value of 10 μW/K measured on copper using a 2ω technique and a thermocouple ThP made of different Wollaston wires [41]. It is also compatible (through Eq. 3) with typical tip-sample interfacial conductance of G_i = 10-35 μW/K and contact radius of 100-200 nm, below 100 °C [42].

5.2. Nanofabricated probe (NThP)

The procedure for the derivation of various conductances of the NThP reported in Table 3 is described in Sections 3.2.2 and 3.2.3. Total conductances G are obtained with Eq. (4), G_p with Eq. (22) and G_{sc} with Eq. (28), using only the NThP data. G_{sa} is determined with Eq. (31), and G_a with Eq. (24) and by using also the PES data (see Section 3.2.3).

Absolute conductance values depend on the first one that is being determined from Eq. (22), $G_p = 5.12$ μW/K, which is in the range of values mentioned in Section 3.2.1. Contrary to the WThP, G_p is the same in different configurations because in the NThP the power source is concentrated in its active zone. Concerning G_{sc}, the value is obtained with the assumption of an isothermal active zone, $\theta_{x=0}/<\theta> = 1$. The maximum temperature gradients in this zone are expected for the ThP suspended in vacuum. A rough estimation of $\theta(x)$ in this situation basing on the integration of infinitesimal $(P/l)dx$ heat sources yielded $\theta_{x=0}/<\theta> = 1.52$. If we take an intermediate value 1.25 for the NThP in contact in ambient air, a corrected value $G_{sc} = 0.807$ μW/K is obtained instead of 1.01 μW/K in Table 3. This correction does not affect the heat flux balance. For comparison, values between 0.24 μW/K [37], 0.35 μW/K [43] and 1.2 μW/K [25] were reported.

Globally, the quantities of Table 3 are complementary to the experimental results obtained in the frequency domain in Ref. [21]. The two experimental data sets agree better with the theoretical parameter estimations therein, if they are recalculated with $h = 635$ Wm^{-2}K^{-1} for the coupling zone (the cantilever), $h = 9040$ Wm^{-2}K^{-1} for the active zone, and if the effective active zone extends two times more into the coupling zone. The latter condition shows that the quasi-isothermal hot part of the probe is larger than strictly the area containing the Pd strip in Fig. 4d. For compar-

Table 2
Experimental values of dc slopes (±10 %), $V_{3\omega}$ and $V_{2\omega}$ signals (effective values ±5 %) from the Wollaston ThP and PE sensor, the average form factor of the temperature profile $<F>$ (±3 %) and thermal conductance results (±15 % absolute error and ±5 % relative error) of various heat exchange channels in different configurations.

Experimental configuration	$(\Delta R/R_0)/P$/W^{-1}	$V_{3\omega}/\mu$V	$V_{2\omega}/\mu$V	$<F>/(-)$	$G/(\mu$W/K)	$G_p/(\mu$W/K)	$G_a/(\mu$W/K)	$G_{sa}/(\mu$W/K)	$G_{sc}/(\mu$W/K)
(V) In vacuum	44.7	-	-	0.333	37.1	37.1	0	0	0
In Argon	36.2	-	-	0.270	45.9	38.6	7.29	0	0
(A) In air	34.4	6.79	0	0.257	48.3	39.0	9.30	0	0
(N) No contact	-	6.234	11.9	0.235	52.6	39.6	3.16	9.75	0
(C) In contact	-	4.438	21.0	0.168	73.8	46.5	3.16	9.75	12.1

Table 3
Experimental values of dc slopes (±10 %), $V_{3\omega}$ and $V_{2\omega}$ signals (effective values ±5 %) from the Nanofabricated ThP and PE sensor, and thermal conductance results (±20 % absolute error and ±5 % relative error) of various heat exchange channels in different configurations.

Experimental configuration	$(\Delta R/R_0)/P/\mathrm{W}^{-1}$	$V_{3\omega}$/mV	$V_{2\omega}/\mu$V	$G/(\mu$W/K)	$G_p/(\mu$W/K)	$G_a/(\mu$W/K)	$G_{sa}/(\mu$W/K)	$G_{sc}/(\mu$W/K)
(V) In vacuum	234	-	-	5.12	5.12	0	0	0
In Argon	188	-	-	6.40	5.12	1.28	0	0
(A) In air	174	9.81	0	6.89	5.12	1.77	0	0
(N) No contact	-	8.61	1.49	7.85	5.12	0.802	1.93	0
(C) In contact	-	7.63	2.01	8.86	5.12	0.802	1.93	1.01

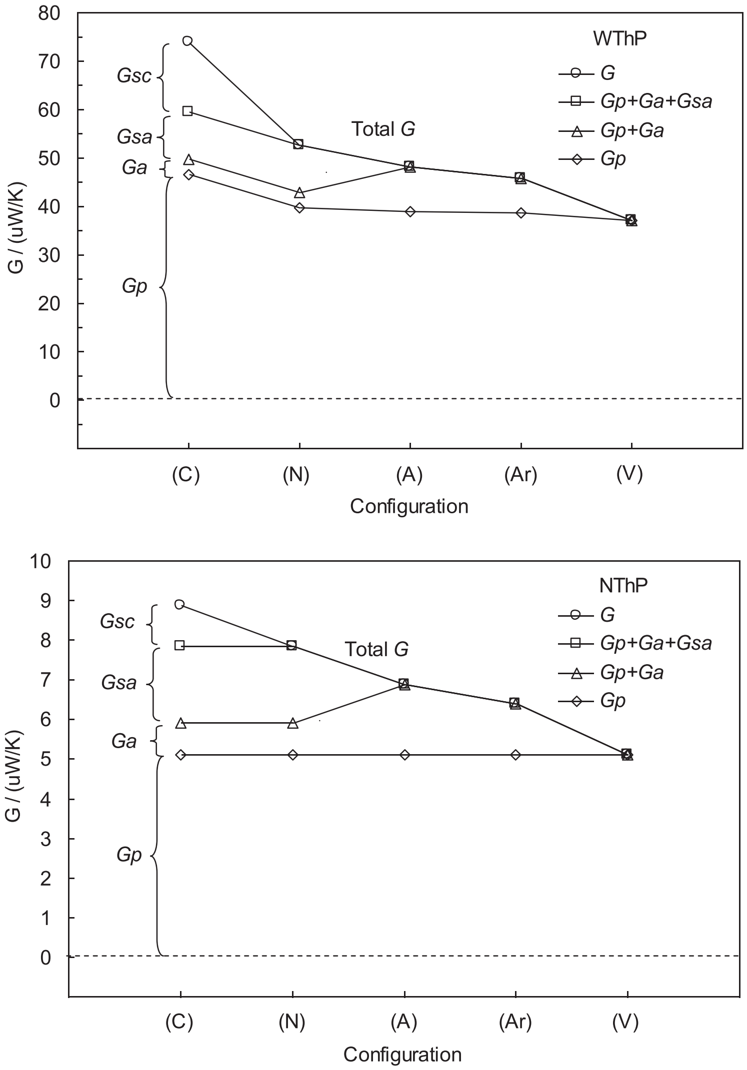

Fig 6. a,b. Histogram of total thermal conductance G and its components, in different tip-sample configurations: in vacuum (V), in Argon (Ar), in air (A), no contact (N) and in contact (C) with the sample.

ison, a value $h = 6100$ Wm^{-2}K^{-1} was determined experimentally [37].

5.3. Comparative discussion of WThP and NThP heat flux balance

The cumulative thermal conductance G of different heat flux exchange channels in ThP-PES systems are plotted in the histograms of Fig. 6a,b, for different configurations. The shares between G_p, G_a, G_{sa} and G_{sc} are also shown, basing on the data from Tables 2 and 3. To make them comparable, G_{sc} has been corrected as in Eq. (15). Conductance G_p of the WThP cantilever is almost constant. G_p of the NThP is assumed constant. Its real variation is expected to be even smaller than the one of the WThP, for the reasons explained at the beginning of Section 3.2.1. Conductance G_a to the ambient air has maximum value in absence of the sample (A), while the conductance G_{sa} through the air to the sample (N, C) is larger than G_a in the same configurations. This is the remote effect or "proximity effect" [26] due to the presence of the sample. The conductance of interest G_{sc} is relatively larger for WThP than for NThP.

Fig. 6a,b show that the effect of the sample is to increase total G by G_{sa} in (A) and (N) configurations, and additionally by G_{sc} in (C) configuration. This suggests two normalization procedures for quantitative SThM measurements, i.e. relative to the tip in air (A), or relative to the tip close to the sample (N). For the studied case the $V_{3\omega}$ signal decrease (cf. Eq. 2) is 34.6 % and 22.2 % [signal (C)/(A)], or 28.8 % and 11.4 % [signal (C)/(N)], for WThP and NThP

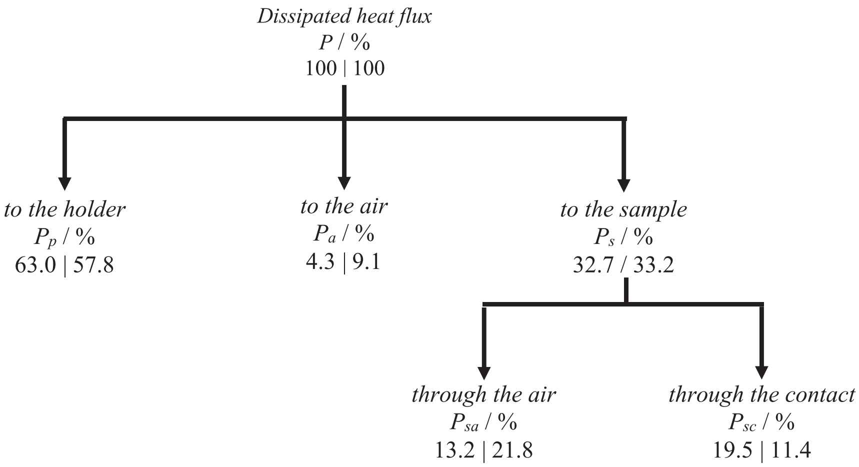

Fig. 7. Heat flux sharing (±5 % of the displayed value) through various channels for Wollaston probe | Nanofabricated probe in contact with a gold-coated pyroelectric sensor (configuration C).

respectively. Since the metrological quantity is G_{sc}, the normalization with the tip just before contact (N) is preferable because it is more sample-specific, despite its lower variation.

Basing on conductance values from Tables 2 and 3, the complete picture of heat flux distribution in the two SThM probe types can be established, in configurations (V, A, N, C). The heat flux conservation law $P = \Sigma(\theta_i G_i)$ is equivalent to $G = \Sigma G_i$ as long as all conductances are connected to the same temperature θ, which is not the case for G_{sc} of WThP. After multiplying G_{sc} by the correction factor $\theta_{x=0}/<\theta> = 1.194$ (see Eq. 15), the heat flux sharing diagram displayed in Fig. 7 is obtained, for tip-sample contact. The error mentioned in the Legend is not affected by the absolute errors of G_i components, but rather by their relative errors.

Literature data susceptible to comparison with those of Fig. 7 are scarce. For the WThP, a heat flux balance computed by finite volume element [13] reports $P_p = 66.0$ %, $P_a = 4.1$ % (of which 0.005 % by radiation transfer) and $P_{sc} = 29.8$ %. An analytical modeling combined with experimental data [35] obtained $P_p = 64$ %, $P_a = 7$ % and $P_{sc} = 29$ %. In these works no distinction is made between P_a and P_{sa}. Using the resistance values of NThP regions calculated in Section 3.2.1., one can derive from the fit of frequency spectra with the ThP in contact with a YAG crystal [21] the fraction $P_{sc} = 11.6$ %.

The total thermal conductance of WThP in air is 7.0 times that of NThP. The conductance G_p of WThP probe alone is 7.2 times larger than that of NThP, which is comparable to factor 10 of their active zone sizes (100 μm / 10 μm). This represents more than half of the heat loss for both ThP types (P_p in Fig. 7).

In absence of the sample, G_a for NThP is roughly proportional to gas thermal conductivity: $G_a(\text{air})/G_a(\text{Ar}) = 1.39$ compared to $k(\text{air})/k(\text{Ar}) = 1.49$. This dependence is weaker for WThP (factor 1.28) because the signal sensitivity to heat loss to air is lower near the two ends of the wire attached to the silver prongs.

The presence of the sample increases the total conductance through air G_a+G_{sa} by 39 % (for WThP) and by 54 % (for NThP). For NThP, the sharing between G_a and G_{sa} is consistent with the geometry of the ThP. Contrary to the WThP, the NThP has a rather flat design. When approaching the sample, the half space above the NThP remains unchanged ($G_a^{N,C} \approx G_a^A/2$), while that below the ThP is reduced to an air gap (which is more conductive than air in free space, having $G_{sa} >> G_a^A/2$). This reasoning applies less to the WThP ($G_a^{N,C} < G_a^A/2$).

Considering Fig. 1, one can imagine the heat flux P_{sa} spreading into a conical shape from the ThP to the surface of the PES. Basing on this, a simplified one-dimensional quantitative interpretation of G_{sa} is possible, which offers an estimation of the lateral extent of this heat transfer channel between ThP and sample. G_{sa} can be considered as the conductance of a cylindrical air gap having a thickness d of half the size of ThP active zone and an equivalent lateral radius given by $r_{Gsa} = (G_{sa} d \pi^{-1} k_{air}{}^{-1})^{1/2}$. The results of 77 μm for WThP and 11 μm for NThP are commensurate with the sizes of the respective heating elements, thus proving that G_{sa} characterizes the whole ThP active zones.

For the studied ThPs, G_{sa} is relatively large. Ignoring it results in assigning this conduction channel either to the one to the ambient air, or to the one of the contact with the sample, depending on the calibration method and on the modeling used. The resulting errors correspond to the P_{sa} fractions in Fig. 7. Since the heat flux channel through G_{sa} has no spatial resolution, its effect on the SThM thermal imaging capability is to blur the thermal contrast of sample structure.

For both ThPs, the sample extracts from the probe a relatively small heat flux fraction P_{sc} (19.5 % for WThP and only 11.4 % for NThP), which is the heat transfer channel of metrological interest. The comparison between P_{sc} and P_{sa} is still in favor of the WThP ($P_{sc} > P_{sa}$), as opposed to the NThP ($P_{sc} < P_{sa}$). The fact that G_{sc} of NThP is 12 times lower than that of WThP is due to much smaller contact radius of the former.

6. Conclusions

This work deals with quantitative analysis of heat transfer mechanisms between two generations of SThM resistive probes (WThP and NThP) and their surroundings basing on experimental data. It is concluded that the heat management in the NThP might be optimized by decreasing the thermal resistance of the active zone and increasing that of the coupling zone. To achieve the latter, the Au coverage of the cantilever substrate should be reduced in a particular region (R_1) close to the heating element. In contrast, the WThP has no coupling zone.

A normalized responsivity S_n is defined which depends only on total conductance G of tip-sample system and which is valid for both dc and ac regimes. S_n is specific for the ThP type but it is independent of experimental parameters such as current, voltage or power excitation. It is suggested that S_n is a convenient measure of sample thermal conductivity in SThM allowing comparisons of measurements performed under different experimental conditions.

Absolute thermal conductance values are comparable to literature data despite broad scatter of reported values which are model-dependent. Heat flux sharing is consistent with few reports on flux balance obtained by simulations. The normalization of SThM signals to the configuration of the tip just before contact (N) is more sample-specific than that of the tip in air far from the sample (A).

The complete heat flux balance of probe-sample system has been established by associating the thermal probes with a pyroelectric heat flux sensor (PES) in place of the sample. The major heat flux channel for both ThP types is the thermal conductance G_p through the cantilever to the probe holder. The second important heat flux channel is that to the air G_a. The presence of the sample modifies the environment, which changes G_a and adds a conductance to the sample across the air gap, G_{sa}. The latter extends beyond the microscopic contact zone and is different from the (ballistic) heat transfer in air across the contact. The disambiguation between the two long-range heat transfer channels in air G_a and G_{sa} was possible owing to the ThP - PES association. For the WThP, G_{sa} is inferior to the contact conductance G_{sc}, while for the NThP, it is twice as large. Finally, the heat flux through the contact G_{sc}, which is of interest, is relatively small if one considers G_a+G_{sa} as a single channel, and the presence of the sample influences the sharing of all heat flux channels.

The weight of G_{sc} in the heat flux balance favors the WThP, but the spatial resolution of the NThP is better due to smaller contact radius. The technological advantage of the NThP is the possibility for batch fabrication, contrary to manual fabrication of the now obsolete WThP. The association of a SThM ThP with a PES represents a new calibration method for ThPs, along with an original data reduction procedure for parameters extraction entirely based on the experiment. The obtained parameter values correspond to a high conductivity sample (63 $Wm^{-1}K^{-1}$ with WThP and 195 $Wm^{-1}K^{-1}$ with NThP). The same calibration scheme might yield parameter values corresponding to a low conductivity sample if using a commercially available polyvinylidendifluoride (PVDF) polymer PES, coated with tens of nm thick metallic electrodes.

Declaration of Competing Interest

None.

CRediT authorship contribution statement

M. Chirtoc: Conceptualization, Methodology, Investigation, Writing - original draft, Writing - review & editing. **J. Bodzenta:** Conceptualization, Methodology, Investigation, Writing - original draft. **A. Kaźmierczak-Bałata:** Conceptualization, Methodology, Investigation, Writing - original draft.

Acknowledgments

The support of the PHC Polonium 2015 Project No. 33564VE is greatly acknowledged. The authors acknowledge ESPEFUM laboratory at Institute of Physics – CSE, Silesian University of Technology for access to SThM facilities. A. K.-B. acknowledges the support of Silesian University of Technology through pro-quality grant (project number 14/990/RGJ18/0101).

References

[1] S. Gomès, A. Assy, P.-O. Chapuis, Scanning thermal microscopy: a review, Phys. Stat. Sol. A 212 (2015) 477–494.
[2] Y. Zhang, W. Zhu, F. Hui, M. Lanza, T. Borca-Tasciuc, M.M. Rojo, A review on principles and applications of scanning thermal microscopy (SThM), Adv. Funct. Mater. (2019) 1900892.
[3] J. Pelzl, M. Chirtoc, R. Meckenstock, Thermal wave-based scanning thermal microscopy and its applications, Int. J. Thermophys. 34 (2013) 1353–1366.
[4] M. Chirtoc, J.-S. Antoniow, J.-F. Henry, P. Dole, J. Pelzl, 1ω, 2ω, 3ω scanning thermal microscopy (SThM) and combinations with thermographic, radiometric, pyroelectric and thermoelastic techniques; principles and applications, Chp. 10, in: J.L. Bubendorff, F.L. Lei (Eds.), Advanced Techniques and Applications on Scanning Probe Microscopy, Transworld Research Network, Trivandrum, Kerala, 2008, pp. 197–247.
[5] E. Gmelin, R. Fischer, R. Stitzinger, Sub-micrometer thermal physics - an overview on SThM techniques, Thermochimica Acta 310 (1998) 1–17.
[6] R. Dinwiddie, R. Pylkki, P. West, Thermal conductivity contrast imaging with a scanning thermal microscope, Therm. Conduct. 22 (1994) 668.
[7] K. Luo, Z. Shi, J. Varesi, A. Majumdar, Sensor nanofabrication, performance, and conduction mechanisms in scanning thermal microscopy, J. Vac. Sci. Technol. B 15 (1997) 349–360.
[8] G. Mills, H. Zhou, A. Midha, L. Donaldson, J.M.R. Weaver, Scanning thermal microscopy using batch fabricated thermocouple probes, Appl. Phys. Lett. 72 (1998) 2900–2902.
[9] G. Mills, J.M.R. Weaver, G. Harris, W. Chen, J. Carrejo, L. Johnson, B. Rogers, Detection of subsurface voids using scanning thermal microscopy, Ultramicroscopy 80 (1999) 7–11.
[10] P.S. Dobson, J.M.R. Weaver, G. Mills, New methods for calibrated scanning thermal microscopy (SThM), Proc. IEEE Sens. (2007) 708–711.
[11] W. Haeberle, M. Pantea, J. Hoerber, Nanometer-scale heat-conductivity measurements on biological samples, Ultramicroscopy 106 (2006) 678–686.
[12] M. Hinz, O. Marti, B. Gotsmann, M.A. Lantz, U. Durig, High resolution vacuum scanning thermal microscopy of HfO_2 and SiO_2, Appl. Phys. Lett. 92 (2008) 043122.
[13] S. Lefèvre, S. Volz, J.B. Saulnier, C. Fuentes, N. Trannoy, Thermal conductivity calibration for hot wire based dc scanning thermal microscopy, Rev. Sci. Instrum. 74 (2003) 2418–2423.
[14] K. Kim, J. Chung, J. Won, O. Kwon, J.S. Lee, S.H. Park, Y.K. Choi, Quantitative scanning thermal microscopy using double scan technique, Appl. Phys. Lett. 93 (2008) 203115.
[15] J. Chung, K. Kim, G. Hwang, O. Kwon, Y.K. Choi, J.S. Lee, Quantitative temperature profiling through null-point scanning thermal microscopy, Int. J. Thermal Sci. 62 (2012) 109–113.
[16] A.A. Wilson, Scanning thermal probe calibration for accurate measurement of thermal conductivity of ultrathin films, MRS Comm. (2019), doi:10.1557/mrc.2019.37.
[17] J. Juszczyk, M. Wojtol, J. Bodzenta, DC experiments in quantitative scanning thermal microscopy, Int. J. Thermophys. 34 (2013) 620.
[18] J. Bodzenta, J. Juszczyk, A. Kazmierczak-Bałata, P. Firek, A. Fleming, M. Chirtoc, Quantitative thermal microscopy measurement with thermal probe driven by dc+ac current, Int. J. Thermophys. 37 (2016) 73.
[19] A. Kazmierczak-Bałata, J. Juszczyk, D. Trefon-Radziejewska, J. Bodzenta, Influence of probe-sample temperature difference on thermal mapping contrast in scanning thermal microscopy imaging, J. Appl. Phys. 121 (2017) 14502.
[20] M. Chirtoc, J.F. Henry, 3ω hot wire method for micro-heat transfer measurements: from anemometry to scanning thermal microscopy (SThM), Europ. Phys. J., Spec. Top. 153 (2008) 343–348.
[21] J. Bodzenta, M. Chirtoc, J. Juszczyk, Reduced thermal quadrupole heat transport modeling in harmonic and transient regime scanning thermal microscopy using nanofabricated thermal probes, J. Appl. Phys. 116 (2014) 054501.
[22] M. Chirtoc, X. Filip, J.F. Henry, J.S. Antoniow, I. Chirtoc, D. Dietzel, R. Meckenstock, J. Pelzl, Thermal probe self-calibration in ac scanning thermal microscopy, Superlatt. Microstruct. 35 (2004) 305–314.
[23] M. Chirtoc, J. Gibkes, R. Wernhardt, J. Pelzl, A. Wieck, Temperature-dependent quantitative 3ω scanning thermal microscopy: local thermal conductivity changes in NiTi microstructures induced by martensite-austenite phase transition, Rev. Sci. Instrum. 79 (2008) 093703.
[24] J. Bodzenta, J. Juszczyk, M. Chirtoc, Quantitative scanning thermal microscopy based on determination of thermal probe dynamic resistance, Rev. Sci. Instrum. 84 (2013) 093702.
[25] Y. Ge, Y. Zhang, J.A. Booth, J.M.R. Weaver, P.S. Dobson, Quantification of probe–sample interactions of a scanning thermal microscope using a nanofabricated calibration sample having programmable size, Nanotechnology 27 (2016) 325503.
[26] J. Spiece, C. Evangeli, K. Lulla, A. Robson, B. Robinson, O.V. Kolosov, Improving accuracy of nanothermal measurements via spatially distributed scanning thermal microscope probes, J. Appl. Phys. 124 (2018) 015101.
[27] A. Assy, S. Gomès, Heat transfer at nanoscale contacts investigated with scanning thermal microscopy, Appl. Phys. Lett. 107 (2015) 043105.
[28] S. Lefèvre, S. Volz, 3ω-scanning thermal microscope, Rev. Sci. Instrum. 76 (2005) 033701.
[29] C. Dames, G. Chen, 1ω, 2ω, and 3ω methods for measurements of thermal properties, Rev. Sci. Instrum. 76 (2005) 124902.
[30] C. Xing, C. Jensen, T. Munro, B. White, H. Ban, M. Chirtoc, Thermal property characterization of fine fibers by the 3-omega technique, Appl. Thermal Eng. 71 (2014) 589–595.
[31] M. Chirtoc, R.M. Candea, V. Mercea, Operation theory of pyroelectric detectors, Ferroelectrics 56 (1984) 283.
[32] M. Chirtoc, E.H. Bentefour, J.S. Antoniow, C. Glorieux, J. Thoen, S. Delenclos, A.H. Sahraoui, S. Longuemart, C. Kolinsky, J.M. Buisine, Current mode versus voltage mode measurement of signals from pyroelectric sensors, Rev. Sci. Instrum. 74 (2003) 648–650.
[33] J.-S. Antoniow, M. Chirtoc, N. Trannoy, O. Raphael, J. Pelzl, Scanning thermal microscopy based on a modified atomic force microscope combined with pyroelectric detection, J. Phys. IV France 125 (2005) 113.
[34] P. Grossel, O. Raphaël, F. Depasse, T. Duvaut, N. Trannoy, Multifrequential ac modeling of the SThM probe behavior, Int. J. Thermal Sci. 46 (2007) 980–988.

[35] S. Gomès, N. Trannoy, P. Grossel, F. Depasse, C. Bainier, D. Charraut, DC scanning thermal microscopy: characterization and interpretation of the measurement, Int. J. Therm. Sci. 40 (2001) 949–958.

[36] https://www.nanowerk.com/nanocatalog/productimages/1441232292Scanning-Thermal-Microscopy-(SThM).pdf, accessed Jun. 11, 2019.

[37] E. Puyoo, S. Grauby, J.-M. Rampnoux, E. Rouvière, S. Dilhaire, Scanning thermal microscopy of individual silicon nanowires, J, Appl. Phys. 109 (2011) 024302.

[38] Kelvin Nanotechnology, https://www.kntnano.com/probes, accessed Jun. 11, 2019, showing second generation of SThM probes.

[39] A.A. Wilson, T. Borca-Tasciuc, Quantifying non-contact tip-sample thermal exchange parameters for accurate scanning thermal microscopy with heated microprobes, Rev. Sci. Instrum. 88 (2017) 074903.

[40] P.-O. Chapuis, E. Rousseau, A. Assy, S. Gomès, S. Lefèvre, S. Volz, Heat transfer between a hot AFM tip and a cold sample: impact of the air pressure, MRS Online Proc. Libr. 1543 (2013) 159–164.

[41] L. Thiery, E. Gavignet, B. Cretin, Two omega method for active thermocouple microscopy, Rev. Sci. Instrum. 80 (2009) 034901.

[42] S. Lefèvre, S. Volz, P.O. Chapuis, Nanoscale heat transfer at contact between a hot tip and a substrate, Int. J. Heat Mass Transf. 49 (2006) 261-258.

[43] I. De, Thermal characterization of nanostructures using scanning thermal microscopy, Univ. Bordeaux (2017) NNT: 2017BORD0563.